atmosphere

MDPI

Article

High-Resolution COSMO-CLM Modeling and an Assessment of Mesoscale Features Caused by Coastal Parameters at Near-Shore Arctic Zones (Kara Sea)

Vladimir Platonov * and Alexander Kislov

Department of Meteorology and Climatology, Lomonosov Moscow State University; Leninskie Gory MGU, GSP-1, 119991 1 Moscow, Russia; avkislov@mail.ru

* Correspondence: vplatonov86@gmail.com; Tel.: +7-903-210-4084

Received: 23 August 2020; Accepted: 3 October 2020; Published: 6 October 2020

Abstract: Coastal Arctic regions are characterized by severe mesoscale weather events that include extreme wind speeds, and the rugged shore conditions, islands, and mountain ranges contribute to mesoscale event formation. High-resolution atmospheric modeling is a suitable tool to reproduce and estimate some of these events, and so the regional non-hydrostatic climate atmospheric model COSMO-CLM (Consortium for Small-scale Modeling developed within the framework of the international science group CLM-Community) was used to reproduce mesoscale circulation in the Arctic coast zone under various surface conditions. Mid-term experiments were run over the Arctic domain, especially over the Kara Sea region, using the downscaling approach, with ≈12 km and ≈3 km horizontal grid sizes. The best model configuration was determined using standard verification methods; however, the model run verification process raised questions over its quality and aptness based on the high level of small-scale coastline diversity and associated relief properties. Modeling case studies for high wind speeds were used to study hydrodynamic mesoscale circulation reproduction, and we found that although the model could not describe the associated wind dynamic features at all scales using ≈3 km resolution, it could simulate different scales of island wind shadow effects, tip jets, downslope winds, vortex chains, and so on, quite realistically. This initial success indicated that further research could reveal more about the detailed properties of mesoscale circulations and extreme winds by applying finer resolution modeling.

Keywords: COSMO-CLM; Arctic wind speed modeling; mesoscale hydrodynamical features; seacoasts; bora; verification

1. Introduction

Arctic climate and extreme weather events have attracted attention recently due to the Arctic amplification of global warming and the accompanying environmental changes. It is well known that the Arctic is the most sensitive region to global climate change, and global temperature increases have been reported to be the highest there [1–3]. The Arctic climate system has many complex feedbacks and teleconnections that manifest in different atmospheric circulation forms [1,4–7], and Arctic warming exceeds the global warming signal, mainly because dynamic processes in the atmosphere provide a poleward heat advection [8].

Sea-ice area decline during the summer season also contributes to polar amplification, and although it is not the main factor [9,10], it facilitates increased extreme wind and wind wave frequencies across the Arctic Ocean region [11,12].

The Kara Sea and surrounding mainland area generally mirror these regional features. Kohnemann et al. have shown [13] maximum winter temperature increases of up to 20 °C, including the surface

layer, north of Novaya Zemlya Island, which were based on COSMO-CLM (Consortium for Small-scale Modeling developed within the framework of the international science group CLM-Community) modeling (15 km resolution) over the Kara region for the period of 2000–2016. As well as its regional effects, Barents–Kara Sea warming affects stratospheric circulation [14], the Arctic Oscillation [15], Eurasian temperature conditions [16–18], and so on, via climate feedback systems.

It is known that many severe atmospheric processes develop initially at the mesoscale, that is, typically exhibiting scales of a few dozen km, and these are referred to as meso-β (meso-beta) scale (20–200 km), and meso-γ (meso-gamma) scale (2–20 km) processes [19]. At the same time, little information has been published on the spatial structures of these features, as the Arctic region is poorly served with ground observation networks. Coastal areas in the Arctic experience the most severe hydrometeorological events, which are caused by the combination of large-scale hydrodynamic conditions, surface properties (tip jets, barrier effects, bora, etc. [20–23]), mesoscale circulations, such as polar lows, cloud microphysics (e.g., polynyas [24]), etc. These events are often an essential part of synoptic-scale systems [25,26]. Severe events can seriously affect coastal ports, transport infrastructure, aviation and airport services [27], and shelf oil and gas production, leading to expensive damage and human casualties.

Satellite data are very useful as spatial information sources, but they are not yet available at either the necessary level of reliability or in sufficient detail or regularity to allow 3D event structure reconstruction. This lack of data means that reanalysis data addressed to mesoscale processes have to be used. In fact, this is the only tool available for obtaining long-term, uniform, hydrometeorological fields detailed in space and time. However, global reanalysis data—such as ERA-Interim [28], NCEP/NCAR [29], MERRA [30], ERA-5 [31], and NCEP-CFSR [32]—have spatial resolutions too coarse to reproduce coastal meteorological processes or the extreme events caused by mesoscale and convection processes adequately.

It is worth mentioning here that Arctic System Reanalysis (ASR) v1 and v2 [33,34] are the only current examples of creating pan-Arctic regional reanalysis long-term timescales (2002–2012). This dataset was achieved by the dynamic downscaling of the ERA-Interim reanalysis, using the polar version of the well-known regional atmospheric model WRF [35] to establish a domain covering the Arctic at a 30 km grid scale (version 2 has a 15 km grid scale). Bromwich et al. [36] noted that ASR reproduced the regimes of most meteorological variables better than the base ERA-Interim reanalysis. It has also been established [37] that the ASR reproduced polar lows better than global reanalyses. On the downside, even if the 15 km grid size allowed the reproduction of features with a horizontal scale of approximately 50 km and more, it could not cover the broad spectrum of severe events at either the meso-γ or more particularly, the meso-β scales.

Despite the clear recent trend to reduce horizontal grid sizes and the appearance of regional reanalyses such as ASR and Russian Academy of Sciences North Atlantic Atmospheric Downscaling (RAS-NAAD) [33,38], the resolutions involved are not sufficient for the needs of the wide range of hydrometeorological information consumers for infrastructure building, conducting Arctic marine operations, or other tasks based on meteorological information. This particularly applies to coastal areas, where there is the highest level of demand.

Considering the numbers of severe events, Arctic coastal development, and the Northern Sea Route prospects, the task of providing detailed hydrometeorological information with horizontal scales of at least several kilometers becomes more acute. Regional climate modeling can provide some assistance here, and there have been studies in the Kara Sea region. These have included the reproduction of polar flow dynamics and their interaction with the ocean, using the Polar version of the WRF-ARW model [39] at 5 km resolution, INMOM model [40], intense storm modeling using the HIRHAM–NAOSIM model [41] at a 0.5° resolution, and so on.

The main goal of the work described in this paper was to investigate the capability of mesoscale, non-hydrostatic models to reproduce atmospheric circulation features over the coastal area of the Kara Sea under conditions of strong winds and diverse surface inhomogeneities, including obstacles,

coastlines, islands, surface-type changes, and many mesoscale features developed in this interaction, according to different spatial scales. The surface 10 m wind speed pattern is focus of this paper, because of more data availability for verification and the use of further model outputs for wave modeling.

The structure of the paper is as follows. The COSMO-CLM model and experimental design are described in the Data and Methods section, with assessment and verification of the modeling results provided in the Results section. In the Discussion section, we have reviewed the ability of the model to reproduce mesoscale effects in coastal areas based on a detailed analysis of strong wind case studies, and we have included suggested interpretations and quantitative estimation of some mesoscale features. The Conclusion section discusses the capacity of the model to reproduce certain event classes and its dependence on spatial resolution and surface properties.

2. Data and Methods

2.1. Model Description

The non-hydrostatic COSMO-CLM model (version 5.0) was the main tool used to simulate atmospheric dynamics in this work. This is a regional mesoscale model developed by the Consortium for Small-scale Modeling (COSMO), which includes some national weather services. The climate version of the model was developed within the framework of the international science group CLM-Community [42]. The main distinctions of this climate model from weather prediction models are modifications and extensions focused on long-term numerical experiments—such as using a deeper soil layer and taking seasonal parameter variations into account [43,44].

The COSMO-CLM model is based on primitive thermo-hydrodynamical equations describing compressible flow in a moist atmosphere. Model equations are solved in rotated latitude–longitude coordinates with a tilted pole, thus minimizing the problem of longitude convergence at the pole. The numerical scheme was implemented on the Arakawa-C grid [45]. For height coordinates, we used the terrain-following, hybrid Gal-Chen coordinate μ (σ–z system), which is an analog of the σ-coordinate from the surface, Z_0, up to an intermediate level, Z_F, and above the Z_F level, it is the simple Z-coordinate [46,47]. This representation of vertical coordinates avoided problems related to surface relief inhomogeneity.

As applied to this work, the standard COSMO-CLM version 5.0 configuration included a two-time level, split-explicit, Runge–Kutta scheme, with acoustic and gravity wave splitting, together with 5th order horizontal advection numerical approximation, Smagorinsky diffusion, a two-stream radiation scheme after Ritter–Geleyn [48], and short and longwave fluxes (employing eight spectral intervals). It also included precipitation formation by bulk microphysics parameterization, including water vapor, cloud water, cloud ice, rain, and snow, with 3D transport for the precipitating phases, as well as Tiedtke mass-flux convection scheme [49] with equilibrium closure, based on moisture convergence for moist and shallow convection. Subgrid-scale turbulence was parameterized using prognostic turbulent kinetic energy closure at level 2.5, including effects from subgrid-scale condensation and thermal circulations. The model also embodied a surface layer scheme based on turbulent kinetic energy, including a laminar-turbulent roughness layer, which allowed the separation of solid surface model values based on a roughness level.

In the model, equations were split into parts associated with acoustic and gravity wave modes and those associated with slow mode atmospheric motions, in order to enhance computation efficiency. This involved evaluating the thermal buoyancy term in the equation for vertical velocity and additional stepping of the heat equation, with respect to the divergence term. The equation subset containing these terms was integrated using the Runge–Kutta scheme of the second order of precision, splitting large time steps onto smaller steps. For applications on the meso-β scale, with horizontal grid spacings of ≈10 km, the gravity wave condition became restrictive; by including gravity wave modes in the reduced set, the stability criterion was shifted to a smaller time step. This extension of the

mode-splitting integration scheme significantly enhanced the efficiency of model applications at the meso-β scale [50,51]. More detailed model descriptions may be found at [52].

External parameters describing some surface properties—including orography, soil properties, Leaf Area Index, Normalized Difference Vegetation Index, and so on—were obtained using the EXTPAR (external parameters) version 5.0 tool [53] from GLOBE (surface orography), MODIS (soil properties and albedo), ECOCLIMAP (forests and plants cover, root depth, land fraction, and many others), and other common datasets.

Model configurations were adopted with specific consideration of Arctic hydrometeorological conditions. In particular, the number of model vertical levels was increased to resolve surface layer processes better (50 levels total, including 10 levels in the surface layer). It was important to be able to reproduce surface wind fields more correctly, which was a major objective of this study, and increasing the vertical resolution contributed to the better reproduction of extreme wind speeds and gusts, whose calculation techniques in the model are quite simple [54,55].

The regional COSMO-CLM model has been proven suited to a broad range of tasks, including modeling high-latitude atmospheric dynamics. It has been applied to polar low dynamics experiments [37,56], for the statistical downscaling of storms over European waters [57], in a CORDEX regional downscaling project [58], and for long-term climate experiments over different areas [59–61], including for the Far East of Russia [62,63] and the Russian Arctic [64].

2.2. Experimental Design

Experiments were carried out using a standard nesting domain scheme; that is, we used the base domain forced by global reanalysis data as initial and boundary conditions, and the nested domain forced by modeling output over the base domain—thus reducing the horizontal grid and time step, as well as the modeling area. The location and cover of the base domain choice represent an important success determinant: firstly, they must cover the entire research area, with a margin to describe large-scale processes from the Kara Sea that influence the main meteorological features there adequately. The domain was enlarged to the N and W, considering the predominance of western motions and northern advections over the region. Moreover, since the model outputs would be used as wave model ADCIRC [65] forcing, some wave-forming patterns in the Kara Sea need to be taken into account. These were clearly defined by large-scale waves on the W boundary coming from the Barents Sea and Northern Atlantic, so we included these regions in the domain area.

ERA-Interim reanalysis data were used as initial and boundary conditions, with a horizontal grid size of 0.7° (≈75 km) [28]; this meant that the base domain resolution had to be no less than 0.10° to obtain the correct downscale ratio. A resolution of 0.12° (≈13 km) was chosen, as had been used widely previously in COSMO-CLM modeling practice [66]. As for the nested domain requirements, they had to be situated deep enough toward the base domain boundaries, and they had to have a resolution up to 8 times less than that of the base domain. In due course, as settled for the model, it covered the entire Kara Sea area, spreading W, with a 0.03° (≈2.8–3 km) grid size, as shown in Figure 1.

The model was run to cover the periods August–October 2012 and July–September 2014; in both cases, the first month was used for a "cold start" only, as it was necessary to adapt the model to the initial conditions, and results from the second and third months were used for analysis. The periods selected for our analyses were characterized by some strong storm events that were objects of interest [67]. The reason of choosing the late summer or early autumn months is that they are the most ice-free [68]. It is simplifying the analysis of surface effects on the wind speed patterns clearly, without any other side impacts. The second reason was concern with the next application of our experiments for wave simulations, for which the ice-free conditions are the most favorable in test runs [68,69].

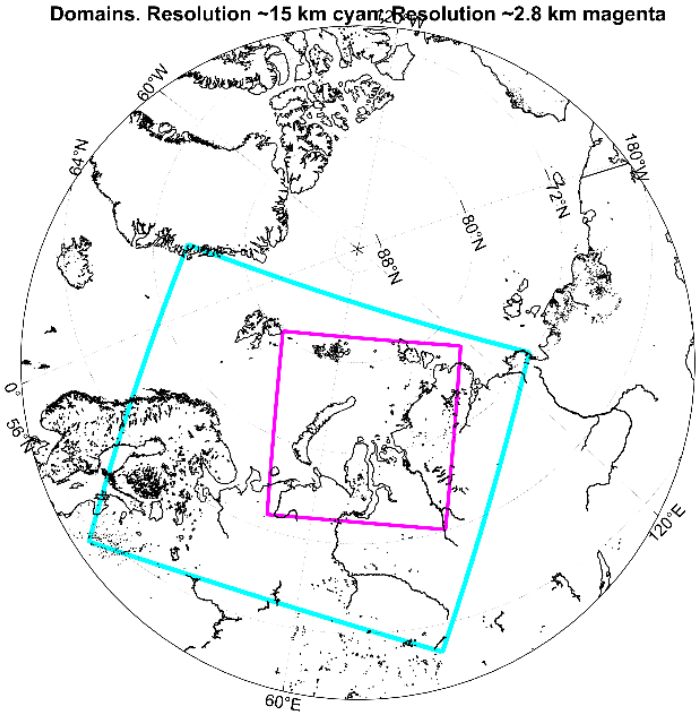

Figure 1. Map of modeling domain boundaries. The base domain is cyan, and the nested domain is magenta.

Interesting storm events were observed over the Kara Sea region during 9–14 October 2012 and 17–23 October 2012. These cases were related to the rapid intensification of a narrow-scaled frontal cyclone centered over the White Sea coast (see Figure S1, Supplementary Materials) and its movement through the Kara Sea (Figure S2, Supplementary Materials). Generally, the 2012 modeling period was characterized by W and NW cyclonic activity, which was intercepted by separate anticyclones from the N and NE. S and SE anticyclonic conditions, as well as N cyclonic conditions, were more frequent during the 2014 modeling period.

The standard model configuration, with its nested domains, was supplemented by versions using the "spectral nudging" technique (further marked as *_sn), the reduced time step, dt (further marked as *_dt), and the enlarged nested domain (further marked as *_large). These changes were suggested by the following considerations. Studies [70–72] have shown that "spectral nudging" contributed to a better assimilation of large-scale meteorological fields, on account of using additional forcing data—in this case, reanalysis. This applied not only at the domain boundaries but also inside the domain, which further restricted the model from departing from real conditions. Accounting for large-scale features was based on two-dimensional Fourier decomposition of meteorological fields from the regional model and reanalysis of regional modeling with subsequent correction. "Nudging" was performed to temperature and wind fields, with 500 km set as the minimal scale for assimilated atmospheric processes from the 850 mb pressure level and above, since middle- and upper-tropospheric circulation systems generally control atmospheric dynamics.

Model time step changes influenced the Courant–Friedrichs–Levy (CFL) numerical criterion, which was crucial for strong wind reproduction: the object of interest in this work [73,74]. Standard experiments were run with a time step (dt) = 100 s and then with reduced time steps (dt) = 80 s (*_dt) over the base domain of ≈13 km, after which both experiments were downscaled to the domain of ≈3 km.

It has been reported that domain boundary changes, that is, domain enlargement or reduction, influence boundary condition information propagation and affect model adaptation to changing boundary conditions [75–77]. In this case, the nested domain, with a horizontal resolution of ≈3 km,

was enlarged to the S on 50 model grids (*_large). This was done to account for continental properties S of the Gulf of Ob, including some considered storm conditions formed in southern streams.

A total of 14 experiments were conducted. The model was run in different configurations for the August–October 2012 and July–September 2014 periods, using the nested domains scheme. All experiments were run using shared high-performance computing resource research facilities (supercomputer "Lomonosov-2" [78]) at Lomonosov Moscow State University.

All listed experiments were verified by surface 10 m wind speeds, using all coastal and inshore meteorological station data over the Kara Sea region and surrounding areas (Figure 2), as available on www.meteo.ru [79]. Verification was carried out using the simple "nearest neighbor" method; that is, station data were compared with those of the nearest station, based on the coordinates model grid, and interpolation methods were not applied. Such an approach was chosen so as not to introduce noise into the model fields and to reveal the impact of surface properties on modeling results. Additional verification of some global reanalyses—namely ERA-Interim [28], NCEP-CFSv2 [32], and ERA5 [31]—was performed using the same technique to compare and estimate the "added value", or contribution, for mesoscale modeling. It should be noted that all stations are located either on the continental coast or on an island in diverse coastline structural conditions and at reliefs of various spatial scales (from km to tens of km). This allowed the effects of surface condition diversity within different sectors, scales, and grid sizes on modeling results to be assessed in detail.

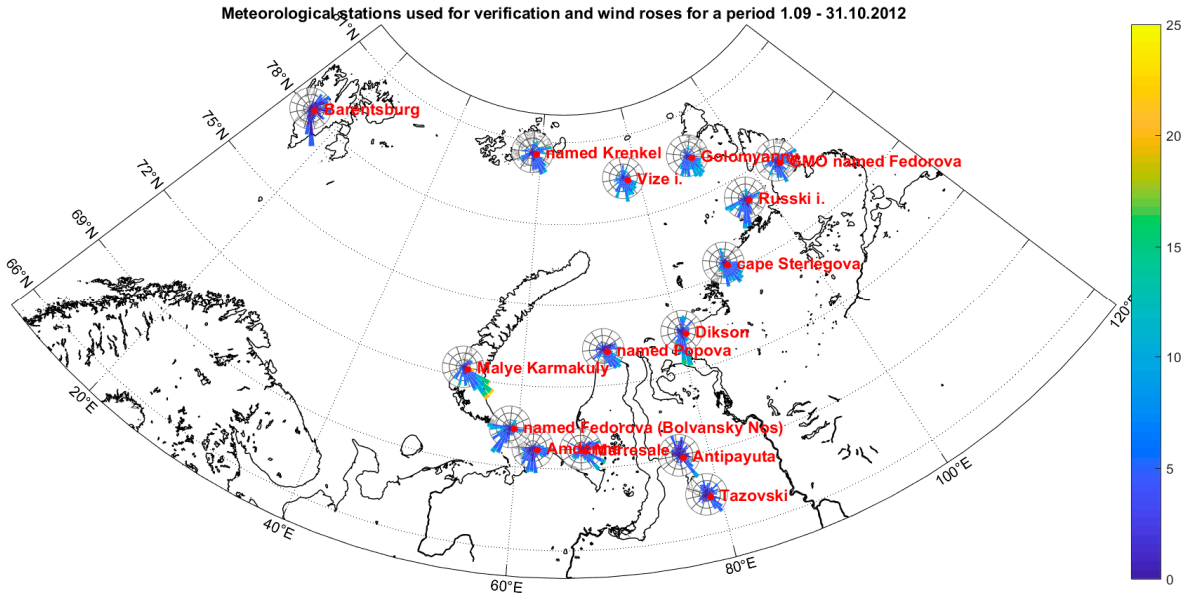

Figure 2. Map of meteorological stations used for experiments verification and increased wind speeds there for the period 1 September–31 October 2012.

3. Results

In this section, we have reviewed the results achieved by all the listed model configurations for both experimental periods, with some statistical outcomes summarized in Tables 1 and 2.

Table 1. Statistical scores of experiments verification results for the September–October 2012 period, 10 m wind.

2012	Correlation Coefficient	Mean Bias, m/s	Median Bias, m/s	RMSE, m/s	STD, m/s
2012 13 km	0.61	0.08	0.04	2.84	2.69
2012 3 km	0.58	−0.51	−0.52	2.85	2.72
2012 13 km sn	0.77	0.13	0.15	2.19	1.96
2012 3 km sn	0.75	−0.01	0.00	2.24	2.17
2012 13 km sn dt	0.78	0.01	0.05	2.17	2.00
2012 3 km sn dt	0.77	−0.09	−0.04	2.15	2.07
2012 3 km sn large	0.76	−0.10	−0.05	2.22	2.13
Reanalyses					
ERA-Interim	0.73	0.39	0.43	2.25	2.05
ERA5	0.79	0.25	0.31	2.05	1.80
NCEP-CFSRv2	0.79	0.43	0.46	2.21	1.98

Table 2. Statistical scores of experiments verification results for the August–September 2014 period, 10 m wind.

2014	Correlation Coefficient	Mean Bias, m/s	Median Bias, m/s	RMSE, m/s	STD, m/s
2014 13 km	0.60	0.46	0.44	2.79	2.68
2014 3 km	0.60	0.46	0.43	2.82	2.73
2014 13 km sn	0.77	0.39	0.41	2.06	1.91
2014 3 km sn	0.72	0.31	0.33	2.25	2.16
2014 13 km sn dt	0.77	0.36	0.35	2.10	1.95
2014 3 km sn dt	0.74	0.31	0.31	2.24	2.15
2014 3 km sn large	0.74	0.29	0.30	2.22	2.14
Reanalyses					
ERA-Interim	0.79	0.39	0.40	1.82	1.72
ERA5	0.78	0.38	0.41	1.75	1.51
NCEP-CFSRv2	0.69	0.52	0.51	2.10	1.96

The standard configuration experiment verification obtained correlation coefficients between wind speed timeseries at stations and the corresponding nearest model grids in the range 0.5–0.7 (0.6 on average) on the base domain, with a ≈13 km grid; for the 2012 period, the worst values were at Russki Island and the named Krenkel stations (≈0.45). Mean biases were quite satisfactory for most stations (less than 1 m/s, with a −0.08 average, except for Cape Bolvanskiy Nos, Antipayuta, and Malye Karmakuly stations), indicating the realistic reproduction of synoptic-scale process dynamics and variability, for two months. Wind speed root mean square errors (RMSEs) were within satisfactory ranges (2.5–3 m/s), except for the above-mentioned stations, which gave values of > 3.5–4 m/s. In particular, large errors at the Malye Karmakuly station were associated with the extreme wind speeds often observed there, which were caused by the well-known Novaya Zemlya Bora [80,81]. Mesoscale processes, highlands, and rugged shorelines contributed significantly to the formation and variability of the downslope winds.

Statistical performance was overall the same for the nested domain; however, the RMSE decreased at some stations, especially at those that had been the highest (mean RMSE was 2.25, compared to 2.84). The same tendency was indicated for biases, and it was also noted that biases and median errors could get negative values for the ≈3 km domain, which could be explained by the fact that mesoscale circulations were reproduced at some locations that were different from the actual observed sites. This problem has been reviewed in the next section.

The 2014-period experiment gave rise to increased biases and median errors up to 0.5 m/s, whereas the RMSEs remained at the same level. The correlation coefficients had a large spread and were all < 0.7 (Antipayuta, Dikson Island), while RMSEs exceeded 3, and even 3.5 m/s, over almost half of the stations (4.4 m/s in Malye Karmakuly).

When we considered the experimental results achieved by the other model configurations, we first noted that the "spectral nudging" technique improved the reproduction of wind speeds in all cases and by all metrics compared to the standard configuration. The mean correlation coefficients increase up to 0.75–0.77, and RMSEs decreased to 2.1–2.2 m/s. This effect was seen across almost all stations: biases were < 1 m/s, except at Antipayuta station, while the RMSE at Malye Karmakuly station decreased to 2.5 m/s for the 2014 period and 3.6 m/s for the 2012 experimental period. The error probability distribution function analysis (see examples in Figure 3) allowed us to conclude that extreme wind speeds could be reproduced better using finer resolution, while background values remained at the same levels. All these results encouraged us to apply the "spectral nudging" technique in our further experiments.

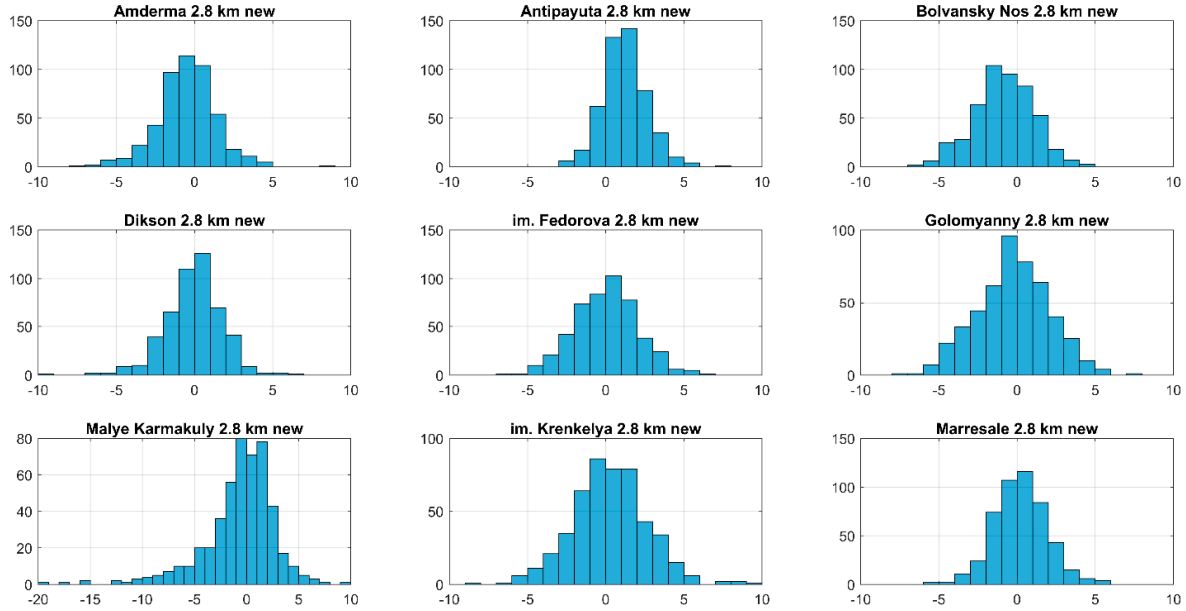

Figure 3. Probability distribution functions of errors at the several stations for the 2012 period experiment "2.8 km _sn".

Reducing the time step (*_dt) elicited an insignificant improvement in the statistical verification metrics, with the 2012 period slightly more concerning. The mean biases were reduced by 0.1 m/s at the base domain, increasing slightly at the ≈3 km grid, while RMSEs decreased clearly (by 0.1) at the finer resolution only. Mean biases decreased slightly for the 2014 experimental period, while the rest of the statistics were at similar levels. The correlation coefficients changed insignificantly in all cases (by < 0.02). Experiments with enlarged nested domains (*_large) demonstrated intermediate results compared to "spectral nudging" and reduced time step experiments, with most variations being insignificant and displaying opposite signs.

The important role of the "spectral nudging" technique in wind speed reproduction has been illustrated using the graphical example in Figure 4, which represents the case at 09:00 GMT on 10 October 2012. A strong SE flow was observed at that time, coming from the Kara Sea and crossing the Novaya Zemlya Island ridges (see Figure S1 of the Supplementary Materials), creating wind speeds up to 25 m/s according to Malye Karmakuly station data. The synoptic conditions were determined by the sea-level pressure (SLP) dipole pattern composed of low pressure over the southern Barents Sea coast and high pressure over the northern Western Siberia. This pattern contributed to the steady strong SE flow. It can be well seen that "spectral nudging" contributed to shifting the area that experienced

the maximum winds (≈20 m/s) much closer to the station location, thus creating a more realistic pattern. It was also apparent that reducing the time step did not change the pattern (Figure 4, right panel). Investigations into using finer resolution and its impact on the reproduction of wind speed and mesoscale circulation, including this example, have been considered in the next section.

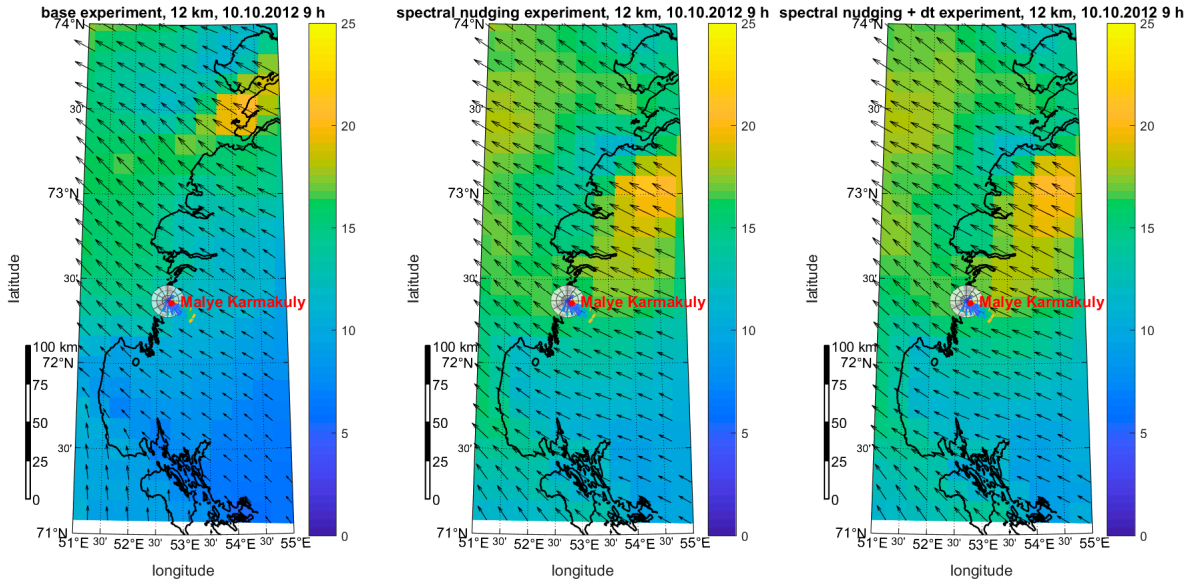

Figure 4. Wind speed (m/s) and direction at the Malye Karmaluly station region on 10 October 2012 at 09:00 GMT for the three experiments with ≈13 km grid (standard, *_sn, *_sn_dt).

Thus, the "spectral nudging" technique was used to improve wind speed reproduction compared to the standard model configuration. Since it plays a significant role in the large-scale conditions' reproduction, the "spectral nudging" is the best choice to assimilate large-scale meteorological fields additionally inside the model domain. At the same time, there was no significant advantage obtained in using reduced time steps, with the improvements achieved being limited to just the second decimal places in the correlation coefficients and biases. Summing these standard verification results, we were able to conclude that the optimal model configuration included "spectral nudging" and time step reduction up to dt = 80 s over the base domain of ≈13 km. Experiments applying this configuration were designated as *_sn_dt.

These verification results raised a question about the comparability of model experimental quality with existing hydrometeorological datasets, such as reanalyses. Three modern, current generation, fine-resolution reanalyses were chosen for comparison—ERA-Interim (0.75°) [28], ERA5 (0.3°) [31], and NCEP-CFSv2 (0.2°) [32]—and the results have been listed in Tables 1 and 2. Reanalysis ERA5 showed the best results for our experimental periods. The best model configuration with "spectral nudging" was of a quality comparable with the reanalyses, but it was slightly less accurate according to most statistics. This result could be explained by the fact that the reanalyses represented the complete assimilation of most available data, including from satellites, while COSMO-CLM uses reanalysis data as forcing only, with no additional data assimilation. At the same time, it should be noted that the obtained scores of the best model configuration agree with estimations of regional climate modeling and reanalyses performance at the Arctic region [82–84]. Therefore, taking these circumstances into account, we could consider our simulation results as quite satisfactory compared to reanalyses.

However, considering the statistics for individual stations, we were able to see that those with the highest errors—such as Antipayuta, Dikson Island, and Malye Karmakuly—corresponded to the worst reanalysis statistics and were worse than the model. In particular, the RMSE for the 2012 test period at Malye Karmakuly station was 4.2 m/s, while the median error at Dikson Island station was 1.6 m/s. This meant that in some cases, the regional model caught the most intense wind speeds

formed by mesoscale processes over the 2-month averaging period better. Taking into account this circumstance, we considered the model experimental results to have been satisfactory and reasonable. The above-mentioned biases could have different sources including model errors, inconsistencies of surface (e.g., land, sea, soil type), altitude, long distance between considered points, and some others. Some cases of strong wind reproduction studied in detail in the Discussion section.

Model resolution refinement led to a reduced error maxima for most stations, and narrowing of the pdf errors, while some stations regularly exhibited high errors. This could be associated with circulation features, such as extreme wind speeds, or with mesoscale surface properties—or even the basic realism of the model. The reproduction of individual case studies using the model gave better results than did reanalysis using coarser resolution. Precise extreme event reproduction, rather than descriptions of averaged parameters, is often the main advantage of mesoscale modeling applications. Our results so far have indicated that a detailed analysis of case studies within different spatial scales for diverse domain regions and experiments should be the next step in our research alongside an attempt to interpret the impact of relief on various coastal zone mesoscale effects.

4. Discussion

Solving the task of realistic wind speed modeling in coastal zones is important, because it is in essence the only data option where there is poor monitoring network coverage. It was clear that the ability of the model to reproduce certain classes of hydrodynamic events was determined by its scale and resolution. Some of these events will be analyzed further, in pursuit of the goal of clarifying the model limitations and its ability to reproduce certain mesoscale effects.

Model wind speed outputs were investigated during storms that occurred over the periods 9–11 October 2012 and 19–20 October 2012, as recorded by the named Popova and Dikson Island stations around Malye Karmakuly, where different obstacle overflows occur, and their effects on the wind regime could be studied. The purpose here was to compare modeling results with meteorological observations.

Airflow interactions with surface objects—such as mountainous terrain, islands, coastlines, and a combination of these factors—cause certain established effects [85]. These can include internal gravity wave [86] and vortex chain formation [87,88], slope catabatic winds, cyclogenesis, and wind shadows [89,90]. These interactions can also give rise to wind speed strengthening over peaks and "corridors" formed by coastlines, horizontal vortex formation behind obstacles [86], wind speed gains from overflowing narrow capes (tip jets) [20], and so on. It should be emphasized that these effects have rarely been documented through field experiments, in numerical solutions with simplified formulations, or in laboratory research. In particular, idealized obstacle shapes and steady stream conditions were considered, which have not been observed in nature.

In this research, we applied the model across a broad spectrum of hydrodynamic effects to simulate real flows traversing obstacles. As prepared, model resolution was sufficiently coarse to not only reconstruct all the effects listed above explicitly but also to measure its integral responses to these effects. In fact, the model needed to be sized with its x, y, and z grid dimensions all at ≈10 m to reproduce internal gravity waves. This was determined by the fact that gravity wave frequency is defined by the Brunt–Väisälä frequency (N ≈0.01 s^{-1}), and the wavelength is determined by the wave scale defined by either the Lyra scale or the inverse Scorer parameter

$$2\pi U/N, \quad (1)$$

where U is the leaking flow velocity.

It was not possible to reproduce vortices in a numerical experiment using a sufficiently coarse resolution. However, the footprint of these structures, when repeated over several obstacle diameters, could be identified as a linearly elongated, enhanced turbulence zone in the coarse grid model. For example, it appeared that under some conditions, it could capture a vortex chain appearance

representing the vortices (generated from both sides) behind the obstacle. This was manifested in the higher turbulence activity of the flow, including enhanced vorticity values.

Wind strengthening along slopes occurs because the wind is not normal to the slope, and thus, the flow is turning more in the corresponding direction. This phenomenon has also been associated with changes in Coriolis force dynamics [91], although the flow needs to transit a sufficiently long fetch along the meridionally elongated slope in order to capture this Coriolis force phenomenon. Issues concerning cyclogenesis and other synoptic-scale processes were not considered in our research for the same reason—that is, they occur beyond the scale of the events that we studied.

The Belyi Island region, where the named Popova station is situated, can be seen in Figure 5. This island, which is approximately 40 km across and flat with no uplands, is separated from the Yamal Peninsula by the 10 km-wide Malygin Strait. The region experienced strong S winds, at ≈15 m/s, on 11 October, 2012, at 1000 h GMT, and this event was established through almost the entire troposphere (see Figure S3a, Supplementary Materials). Such steady flow was caused by a combination of the deep cyclone centered over the White Sea and the Siberian high. By analyzing the *sn_dt experiment with a ≈3 km grid (Figure 5), we saw wind speed reduced over the island and observed the wind shadow phenomenon with a significant wind speed reduction (by 5 m/s and more) on the leeward (N) coast. This zone extended out over the sea for 20–30 km, and the island was framed by jets of different intensities and with widths between 10 and 20 kms. It should be noted that the observed wind speeds at 10 m height were 11–13 m/s, which were only 1–2 m/s above the modeled velocities. These results showed us that the COSMO-CLM model could capture events at the spatial scale of islands, changes in surface type (land–sea), island impacts on wind field structure, and interactions with the sea.

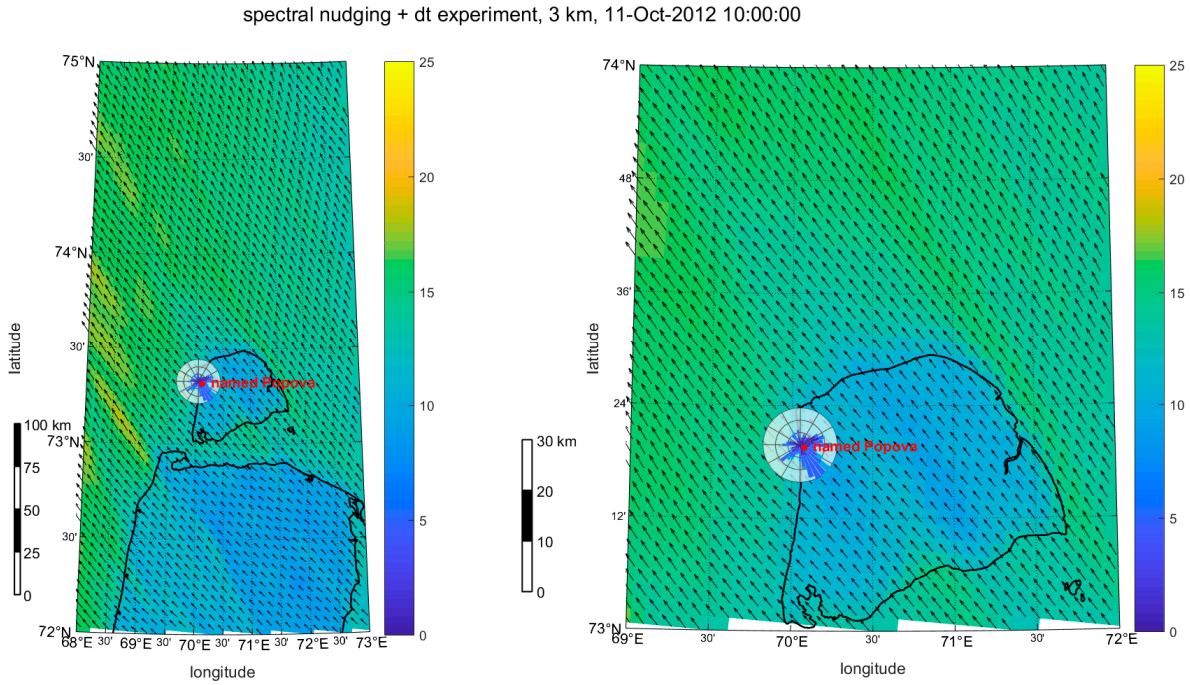

Figure 5. Wind speed (m/s) and direction at the named Popova (Belyi Island) station region on 10 October 2012, 900 GMT for the experiment ≈3 km grid, *_sn+dt. Right panel is the enlarged version of the left panel.

The relative vorticity pattern (Figure 6) was determined by elongated alternating bands of positive and negative values, which were 100 km or more long and up to 10 km wide. These bands were distinguishable by given ≈3 km grids—that is, they could be determined by at least four grid points considering the relative vorticity calculation technique. This was unrelated to the influence of the island itself, except for one feature—the manifestation of positive vorticity maxima on the E coast.

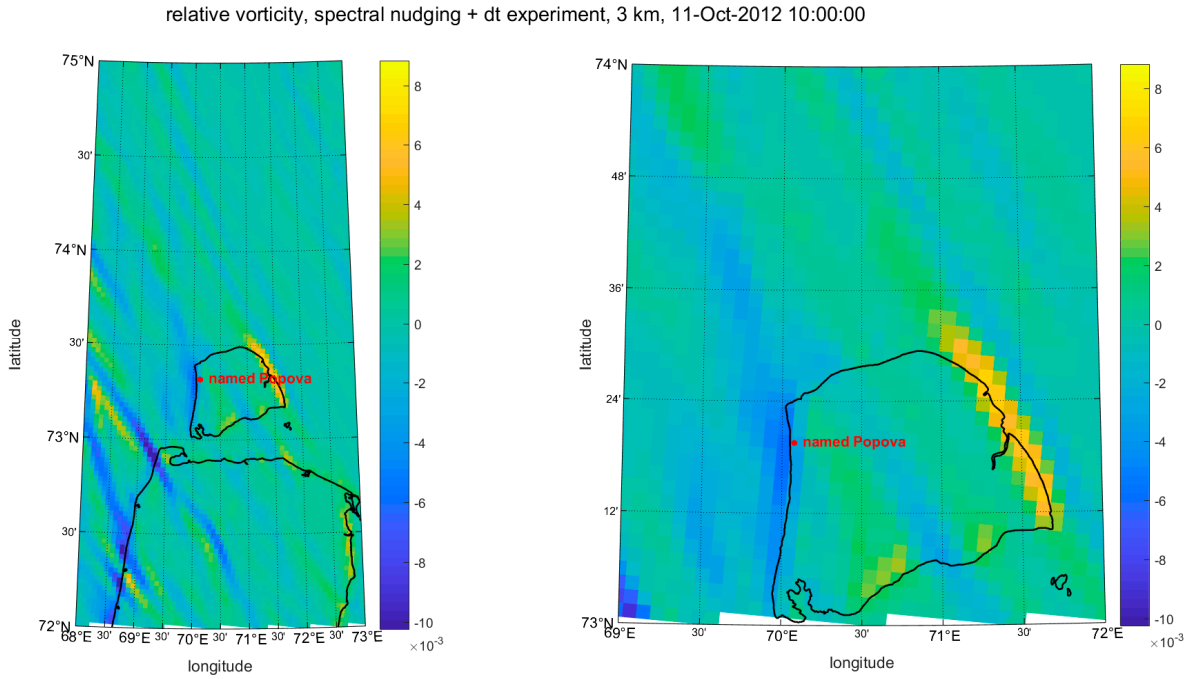

Figure 6. Relative vorticity (10^{-3} m/s^2) for the *_sn+dt experiment ≈3 km grid, on 11 October 2012, at 10:00 GMT, at the named Popova (Belyi Island) station region. The right panel is the enlarged version of the left panel.

In considering how to explain this phenomenon, we introduced natural coordinates t and n [92]. In this solution, unit vector t was oriented parallel to the horizontal velocity at each point, while unit vector n was normal to the horizontal velocity and oriented so as to be positive to the left of the flow direction. The relative vorticity in such coordinates would be defined as

$$\xi = -\frac{\partial V}{\partial n} + \frac{V}{R} \quad (2)$$

Here, R denotes the radius of curvature following the parallel motion. It followed that decreasing the wind speed module by transition from the background sea flow to the shadow zone should have led to an intensification of cyclonic vorticity. It was interesting that on the island W coast, the corresponding effect of an opposite sign, that is, intensification of anticyclonic vorticity, was expressed only weakly; the possible reason for this difference could have been that there was no advection of the necessary vorticity inbuilt into the oncoming flow.

The existence of elongated vortices of opposite signs alternating inside the flow could be presented as a manifestation of vortex chains—and these were not those Karman vortex streets related genetically to the flow around islands. This phenomenon reminded us of narrow zones of higher wind speeds in turbulence flows, which are sometimes referred to as "strings". Their generation and disappearance originate from dissipation bursts associated with the turbulence intermittency process, namely, irregular autofluctuations of flow with magnitudes comparable with the flow speed itself [93–95]. Although the genesis of this phenomenon is completely different from that considered here, the similarity of patterns manifesting in coherent structural formations has been attracting attention.

In the second example, we considered wind behavior at the E Kara Sea coast in the vicinity of the Yenisey Gulf, looking at Sibiryakov and Dikson islands (the latter having dimensions of 3–4 km). Dikson Island is separated from the Taymyr Peninsula by a narrow (1–2 km) strait (Figure 7) and features rocky terrain (unlike Belyi Island), although this terrain does not rise above 25 m.

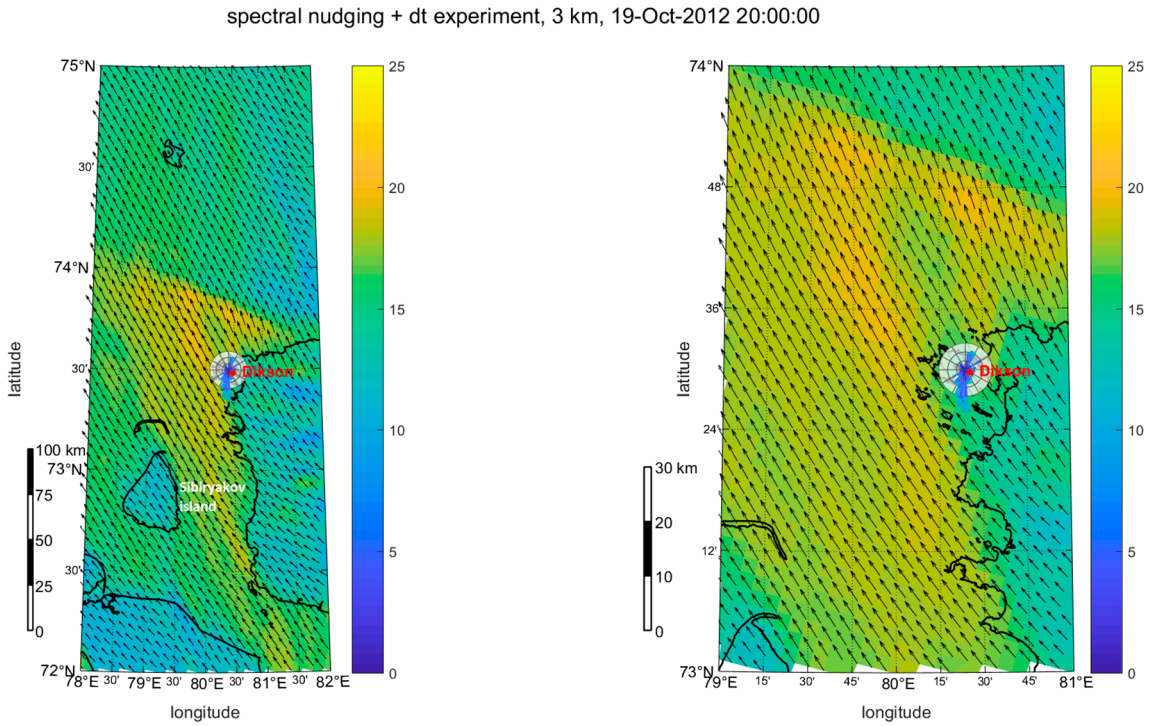

Figure 7. The same as in Figure 5, for the Dikson Island station region, 19 October 2012, at 20:00 GMT.

Steady strong winds exceeding 20 m/s were observed for many hours at the Dikson Island station on 19–20 October 2012. The synoptic conditions were characterized by steady S flow (15 m/s and more) within a layer up to 600 mb, as shown in Figures S2 and S3b of the Supplementary Materials, and they were caused by dipole SLP structures, including a cyclone centered over the Kara Sea and an anticyclone over the N of Eastern Siberia. The model reproduced strong airflow over the sea from the Yenisey Gulf, showing that it was disturbed by a large Sibiryakov Island's wind shadow (wind speed decreased by 10 m/s). It was noted that wind speeds were reduced less (by 5 m/s) in the wind shadow of the smaller Dikson Island and other small islands nearby.

A significant wind speed increase was seen in the Dikson stream (>20 m/s), which had a width of up to 10 km. Its formation was determined by the declining friction force there, as well as by the rocky coastal terrain, creating a peculiar wind corridor, and we noted that the stream conserved its shape at the exit from the strait. The observed wind speeds were 21–23 m/s, which corresponded to the stream wind speed reproduced by the model.

Vorticity pattern analysis (Figure 8) illustrated this vorticity band alternation of opposite signs inside the flow. Cyclonic vorticity maxima were noted again along the E coasts of Sibiryakov and Dikson islands, and they were analogous to that considered in Belyi Island, although the effect of the anticyclonic vorticity maximum appeared on the W coast of the larger Sibiryakov Island.

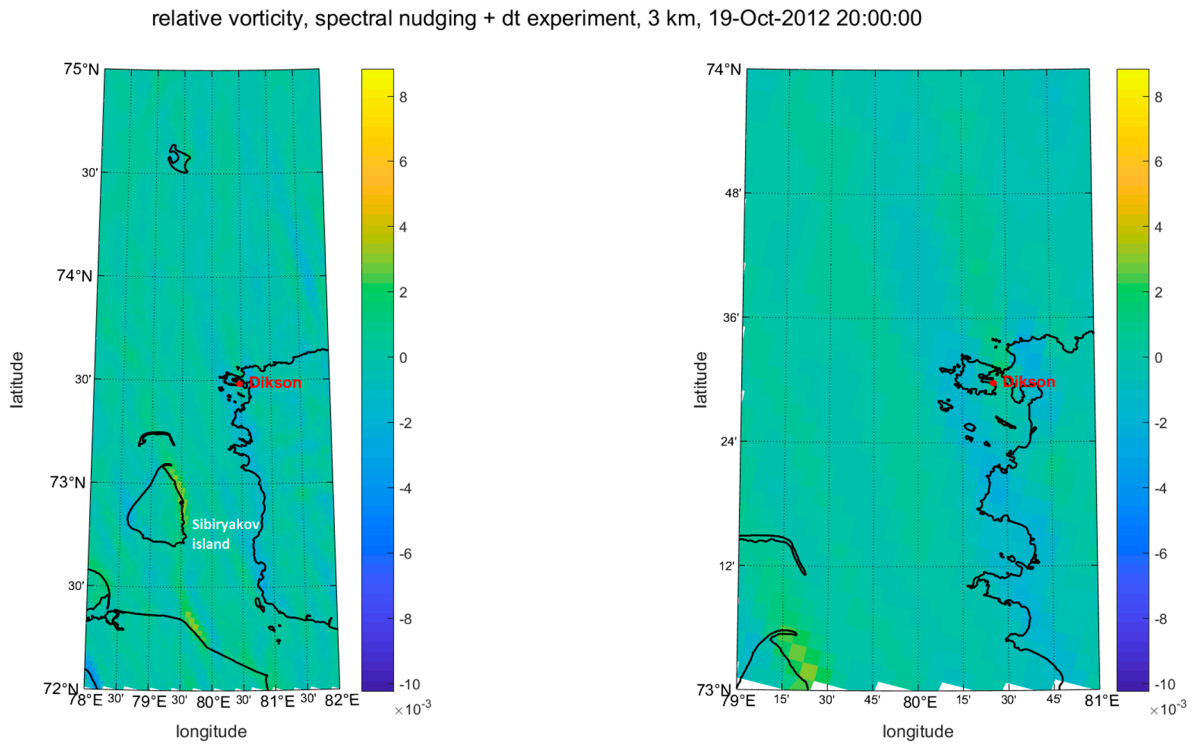

Figure 8. The same as in Figure 6, for the Dikson Island station region, on 19 October 2012, at 20:00 GMT.

We also considered a case study of strong winds on the W coast of Novaya Zemlya Island on 10 October 2012, as observed at Malye Karmakuly station. We had noted before that the highest wind speeds over the Eurasian Arctic are observed at Novaya Zemlya [96,97]. This region is characterized by the presence of bays, bights, rugged shores, and a 700 m + mountain range standing a few km inland. Such terrain favors katabatic stock wind formation (such as the Novaya Zemlya Bora), which is strengthened over different coastal features. Theoretical approaches based on simplified models of the dynamic interaction of the incoming flow with topography, such as hydraulic and wave approaches, have been widely used to describe downslope windstorms [98]. This and other early results have been confirmed by mesoscale modeling data in some respects [80,99], where a successful attempt has been made to explain small-scale, non-modeling explicit processes by applying integral hydrodynamic parameters.

The experimental ≈3 km grid, using "spectral nudging", obtained realistic results in our study, corresponding to measurement data for Malye Karmakuly station. The maximum modeled wind speed (25 m/s) was observed over the entire length of the station's bight (Figure 9), and there was quite clear wind speed enhancement down the leeward slope.

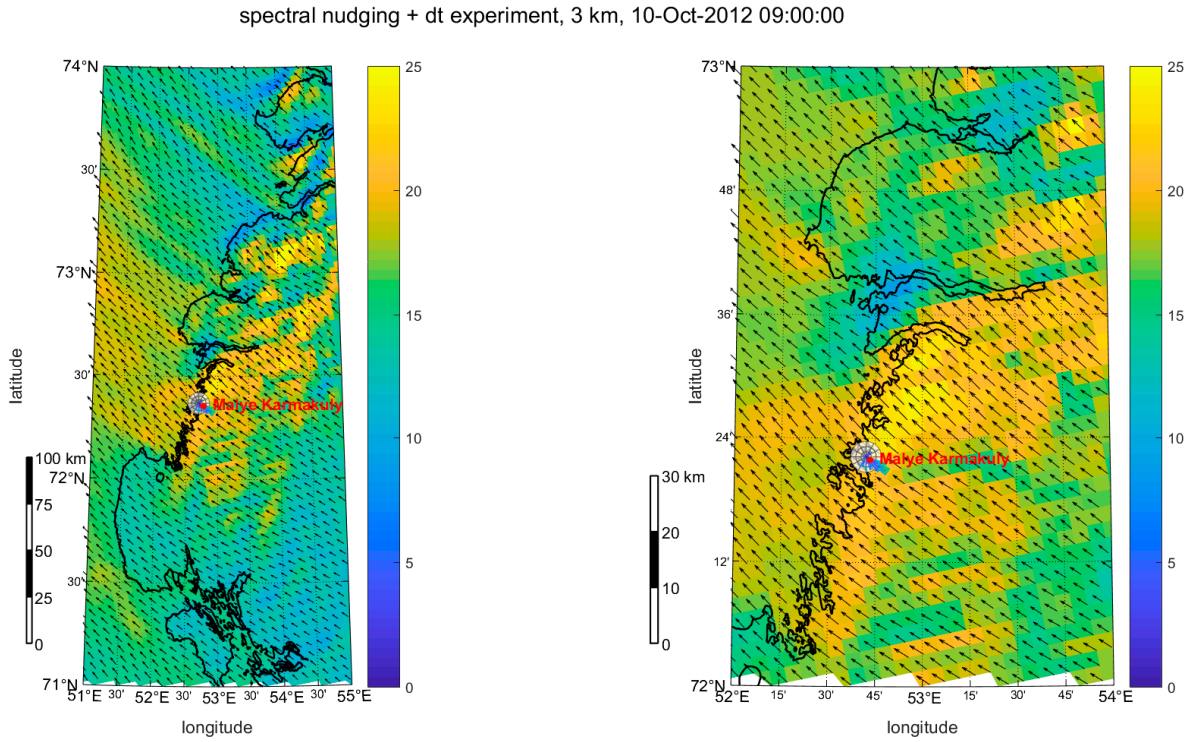

Figure 9. Wind speed (m/s) and direction at the Malye Karmakuly station region, on 10 October 2012, at 09:00 GMT for the ≈3 km experiment, *_sn_dt. Right panel is the enlarged version of the left panel.

The wind speed pattern became less homogeneous as it came ashore, reflecting the inhomogeneity of the background flow, as well as the influence of the complicated coastline configuration. It should be noted that these effects were not apparent in the ≈13 km grid experiment, showing that the model responded to more detailed surface descriptions. The wind shadow was not clearly pronounced. Ten to 20 km-wide streams were evident, as in previous examples, as well as areas of significantly lower wind speed (by 10–15 m/s), which were stretched along river valleys, with the latter wind speed reduction most likely associated with valley surface roughness.

Airflow perturbation is a characteristic feature of bora and downslope winds, and the wind speed module standard deviation has usually been used to replicate the natural turbulence metric. This quantity was calculated over the period of the feature's existence (≈21 h)—that is, for a period of steady SE flow—and showed that flow turbulence reached its maximum over the Novaya Zemlya shore, as evidenced by the highest speed tip bands being immediately adjacent to the coast (Figure 10).

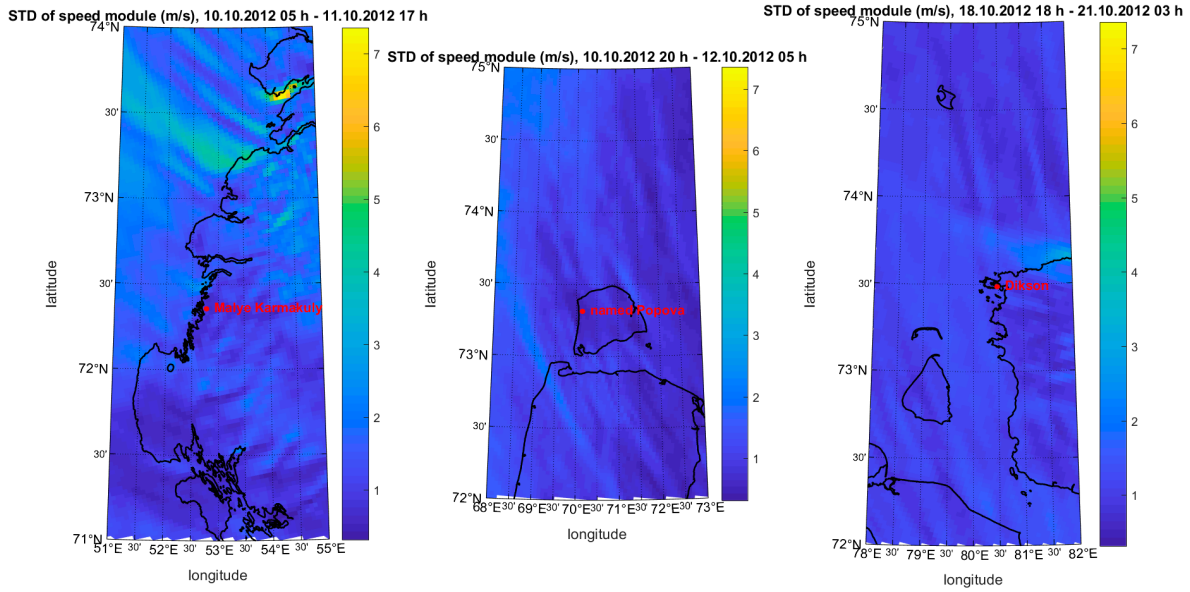

Figure 10. Standard deviation of wind speed module (m/s) for 21, 30, and 17 h periods at three considered regions, ≈3 km grid.

The relative vorticity pattern can be seen in Figure 11. Cyclonic and anticyclonic vorticity areas were clear, with horizontal diameters of 10–30 km and with strong vorticity gradients over land corresponding to stock downslope winds. Linearly stretched vorticity zones of the same sign were quite clear again; they extended for > 100 km, were 10–15 km wide, and were probably enhanced by tip jets. Vorticity bands could also be traced in river valleys.

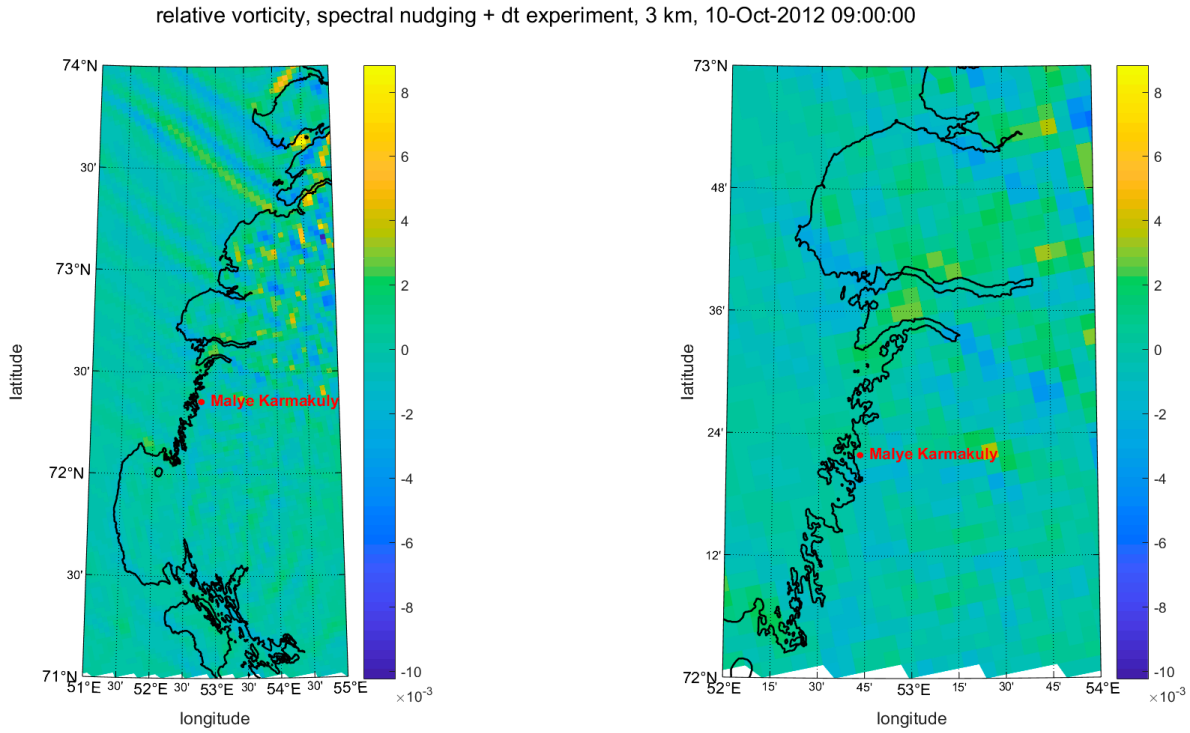

Figure 11. The same as in Figure 6, for the Malye Karmakuly station region on 10 October 2012 at 09:00 GMT.

It was clear to us that transition to a more detailed surface description played a key role in the model's ability to simulate actual wind patterns. The model showed itself to be capable of reproducing

downslope windstorms, although the physical mechanisms responsible for this bora phenomenon could not yet be completely implemented in the model.

The mesoscale strong wind speeds modeled in the case studies were compared to global reanalysis data ERA5 and NCEP-CFSv2 for the experimental periods, with the results available in Figures S4 and S5 of the Supplementary Materials. These comparisons clearly showed that the differences in surface wind patterns were caused by using a coarser grid, which resulted in surface wind descriptions that were not as good as those of the reanalyses. However, as mentioned above, when case studies of extreme events were simulated by the mesoscale model, the results were significantly better in comparison with the reanalysis data.

5. Conclusions

The principal task of this research was to review the capability of the mesoscale model, COSMO-CLM, to reproduce sophisticated atmospheric circulation features related to the impact of surface properties on airflow. The main focus of the study was on high-latitude atmospheric dynamics, which have been closely reviewed in this paper. The investigation focused on the developing influence of obstacles, such as islands and moderately mountainous terrain, on the mesoscale processes in the atmosphere. The authors were aware that a horizontally gridded model with a scale of just a few km would not be capable of explicitly reproducing the entire spectrum of such dynamic effects, and they kept in mind that internal gravity waves were manifested in different meteorological phenomena, such as wind speed acceleration within downslope flows and circulation vortex chain formation. At the same time, we expected to detect integral effects at least, as gravity wave effects were parametrized in the model as wave resistance manifested as flow around surface obstacles.

From another point of view, well-known ideas about the physical phenomena resulting from flow around obstacles were reproduced using significantly simplified approaches. Therefore, the analysis achieved within the framework of the physically detailed COSMO-CLM model was still able to improve our event representations, despite the capability limitations mentioned above.

Analysis of model patterns showed that the mesoscale features appeared clearly on a ≈3 km grid in all the cases that were examined. In contrast, the same features either were or were not revealed by the ≈13 km grid, often appearing either indistinctly or not at all—or being translocated. This suggested that the model captured details adequately and allowed us to expect that coastal mesoscale circulations could be reproduced quite reliably. This is important for applications such as pollution calculation, coastal wind wave simulation, and so on.

The successful reproduction of mesoscale streams alternating inside a flow, that is, elongated bands of cyclonic and anticyclonic vorticity, was an important outcome from this work. We also showed that the model could reflect mesoscale circulation organization, in the form of a certain rotation vortex system (known as a hydrodynamic property of flow), and that these bands were not related to relief. The influence of obstacles met in a wind path manifests in vorticity enhancement (of the corresponding sign) on coasts, as flows wrap themselves around the obstacles. Flow organization in the form of vorticity zones called to mind the phenomena known as "intermittency zones", or "streams", which have been distinguished in turbulence flows.

Simulating flow around islands illustrated wind shadow production, whose parameters were influenced by surface roughness. These phenomena were found to extend along the flow by more than simply the size of the island, and this is an effect worthy of future research, using islands of different shapes and sizes.

Wind speed and turbulence strengthening were reproduced at the leeward base of over mountain flows, reflecting the main features of downslope wind development (the Novaya Zemlya Bora phenomenon). Moreover, although the model could not reconstruct all wind event mechanisms, those phenomena that it did simulate showed characteristics close to reality.

We noted that the high-resolution COSMO-CLM model created realistic patterns at the expense of imitation mechanisms defined by subgrid process parameterizations. Our results suggested that

mesoscale modeling could be a reliable source of information on mesoscale circulations in areas such as the Arctic, where there are few weather observation platforms.

Modeling verification results should be considered critically with respect to the "nearest neighbor" technique, concerning the above-mentioned conclusion. Indeed, since station data are irreplaceable for local environmental and geographic conditions, and model simulations cannot fully replicate natural patterns, the usefulness of comparing model data with station observations becomes moot at a certain point. This implied that the further development of verification techniques, moving away from the direct grid–station point comparisons, is needed.

Model capability in reproducing some wind patterns reliably and physically, including extreme winds, will really help investigation into the physical description of these objects by applying different hydrodynamical parameters. We have shown that existing global and regional reanalysis data are unable to describe severe weather event patterns in coastal regions, although they can surpass mesoscale modeling with respect to mean climatic statistics. Reanalysis data will also facilitate the future use of regional climate models, with horizontal grid steps of just a few kilometers, to carry out adequate high-resolution wind climatological assessments, in conditions where other hydrometeorological information sources are absent. These studies could have wide applications in resolving actual tasks associated with estimating Arctic climate change. The work described in this paper will be continued in this direction by studying the quantitative parameters of mesoscale effects, assessing the influence of coastline characteristics, measuring the impact of terrain on wind properties, and so on.

Supplementary Materials: The following are available online at http://www.mdpi.com/2073-4433/11/10/1062/s1, Figure S1: Surface analysis and AT500 map on 10 October 2012, at 0000 GMT, source: GFS. Color represents the 500 mb geopotential height (gpdam), white lines are isobars of surface pressure (hPa), Figure S2: Surface analysis and AT500 map on 20 October 2012, at 0000 GMT, source: GFS. Color represents the 500 mb geopotential height (gpdam), white lines are isobars of surface pressure (hPa), Figure S3: Atmospheric soundings: (a) at Naryan-Mar on 11 October 2012, at 0000 GMT; (b) at Dikson Island on 19 October 2012, at 1200 GMT, Source: University of Wyoming, Figure S4: Wind speed (m/s) and direction based on the ERA5 data over three regions, Figure S5: Wind speed (m/s) and direction based on the NCEP-CFSv2 data over three regions.

Author Contributions: Conceptualization, V.P. and A.K.; methodology, V.P. and A.K.; software, V.P.; validation, V.P.; formal analysis, V.P. and A.K.; investigation, V.P. and A.K.; resources, V.P.; data curation, V.P.; writing—original draft preparation, V.P; writing—review and editing, V.P. and A.K.; visualization, V.P.; supervision, A.K. and V.P.; project administration, A.K.; funding acquisition, A.K. All authors have read and agreed to the published version of the manuscript.

Funding: The reported study was funded by RFBR according to the research project № 18-05-60147 and Lomonosov Moscow State University project no. AAAA-A16-116032810086-4. The APC was funded by the RFBR research project № 18-05-60147.

Acknowledgments: The research is carried out using the equipment of the shared research facilities of HPC computing resources at Lomonosov Moscow State University. Authors also acknowledge the CLM-Community and COSMO Consortium.

Conflicts of Interest: The authors declare no conflict of interest.

References

1. Stocker, T.F.; Qin, D.; Plattner, G.-K.; Tignor, M.M.B.; Allen, S.K.; Boschung, J.; Nauels, A.; Xia, Y.; Bex, V.; Midgley, P.M.; et al. Climate change 2013: The Physical Science Basis. Contribution of Working Group I to the Fifth Assessment Report of the Intergovernmental Panel on Climate Change. 2013. Available online: https://www.ipcc.ch/site/assets/uploads/2018/03/WG1AR5_SummaryVolume_FINAL.pdf (accessed on 23 August 2020).
2. Johannessen, O.M.; Kuzmina, S.; Bobylev, L.P.; Miles, M.W. Surface air temperature variability and trends in the Arctic: New amplification assessment and regionalization. *Tellus* **2016**, *68A*, 28234. [CrossRef]
3. Walsh, J.E. Intensified warming of the Arctic: Causes and impacts on middle latitudes. *Glob. Plan. Change* **2014**, *117*, 52–63. [CrossRef]
4. Budikova, D. Role of Arctic sea ice in global atmospheric circulation: A review. *Glob. Plan. Change* **2009**, *68*, 149–163. [CrossRef]

5. Mori, M.; Watanabe, M.; Shiogama, H.; Inoue, J.; Kimoto, M. Robust Arctic sea-ice influence on the frequent Eurasian cold winters in past decades. *Nat. Geosci.* **2014**, *7*, 869–873. [CrossRef]
6. Overland, J.; Francis, J.A.; Hall, R.; Hanna, E.; Kim, S.J.; Vihma, T. The melting Arctic and midlatitude weather patterns: Are they connected? *J. Clim.* **2015**, *28*, 7917–7932. [CrossRef]
7. Screen, J.A.; Deser, C.; Simmonds, I. Local and remote controls on observed Arctic warming. *GRL* **2012**, *39*. [CrossRef]
8. Cohen, J.; Screen, J.A.; Furtado, J.C.; Barlow, M.; Whittleston, D.; Coumou, D.; Francis, J.; Dethloff, K.; Entekhabi, D.; Overland, J.; et al. Recent Arctic amplification and extreme mid-latitude weather. *Nat. Geosci.* **2014**, *7*, 627–637. [CrossRef]
9. Vihma, T. Effects of Arctic sea ice decline on weather and climate: A review. *Surv. Geoph.* **2014**, *35*, 1175–1214. [CrossRef]
10. Bekryaev, R.V.; Polyakov, I.V.; Alexeev, V.A. Role of polar amplification in long-term surface air temperature variations and modern Arctic warming. *J. Clim.* **2010**, *23*, 3888–3906. [CrossRef]
11. Barnes, E.A. Revisiting the evidence linking Arctic amplification to extreme weather in midlatitudes. *GRL* **2013**, *40*, 4734–4739. [CrossRef]
12. Francis, J.A.; Vavrus, S.J. Evidence linking Arctic amplification to extreme weather in mid-latitudes. *GRL* **2012**, *39*. [CrossRef]
13. Kohnemann, S.H.; Heinemann, G.; Bromwich, D.H.; Gutjahr, O. Extreme warming in the Kara Sea and Barents Sea during the winter period 2000–16. *J. Clim.* **2017**, *30*, 8913–8927. [CrossRef]
14. Zhang, P.; Wu, Y.; Simpson, I.R.; Smith, K.L.; Zhang, X.; De, B.; Callaghan, P. A stratospheric pathway linking a colder Siberia to Barents-Kara Sea sea ice loss. *Sci. Adv.* **2018**, *4*, eaat6025. [CrossRef] [PubMed]
15. Yang, X.Y.; Yuan, X.; Ting, M. Dynamical link between the Barents–Kara sea ice and the Arctic Oscillation. *J. Clim.* **2016**, *29*, 5103–5122. [CrossRef]
16. Petoukhov, V.; Semenov, V.A. A link between reduced Barents-Kara sea ice and cold winter extremes over northern continents. *J. Geoph. Res. Atmos.* **2010**, *115*. [CrossRef]
17. Kug, J.-S.; Jeong, J.-H.; Jang, Y.-S.; Kim, B.-M.; Folland, C.K.; Min, S.-K.; Son, S.-W. Two distinct influences of Arctic warming on cold winters over North America and East Asia. *Nat. Geosci.* **2015**, *8*, 759–762. [CrossRef]
18. Outten, S.D.; Esau, I. A link between Arctic sea ice and recent cooling trends over Eurasia. *Clim. Chang.* **2012**, *110*, 1069–1075. [CrossRef]
19. Orlanski, I. A rational subdivision of scales for atmospheric processes. *BAMS* **1975**, *56*, 527–530.
20. Moore, G.W.K.; Renfrew, I.A. Tip jets and barrier winds: A QuikSCAT climatology of high wind speed events around Greenland. *J. Clim.* **2005**, *18*, 3713–3725. [CrossRef]
21. Shestakova, A.A. Novaya Zemlya bora: The lee characteristics and the oncoming flow's structure. *Arct. Antarct.* **2016**, *2*, 11–22. [CrossRef]
22. Christakos, K.; Furevik, B.R.; Aarnes, O.J.; Breivik, Ø.; Tuomi, L.; Byrkjedal, Ø. The importance of wind forcing in fjord wave modelling. *Ocean. Dyn.* **2020**, *70*, 57–75. [CrossRef]
23. Kilpeläinen, T.; Vihma, T.; Manninen, M.; Sjöblom, A.; Jakobson, E.; Palo, T.; Maturilli, M. Modelling the vertical structure of the atmospheric boundary layer over Arctic fjords in Svalbard. *Q. J. R. Met. Soc.* **2012**, *138*, 1867–1883. [CrossRef]
24. Khvorostyanov, V.I.; Curry, J.A.; Gultepe, I.; Strawbridge, K. A springtime cloud over the Beaufort Sea polynya: Three-dimensional simulation with explicit spectral microphysics and comparison with observations. *J. Geophys. Res.* **2003**, *108*, 4296. [CrossRef]
25. Gutjahr, O.; Heinemann, G. A model-based comparison of extreme winds in the Arctic and around Greenland. *Int. J. Clim.* **2018**, *38*, 5272–5292. [CrossRef]
26. ReVelle, D.O.; Nilsson, E.D. Summertime low-level jets over the high-latitude Arctic Ocean. *J. Appl. Met. Clim.* **2008**, *47*, 1770–1784. [CrossRef]
27. Gultepe, I.; Sharman, R.; Williams, P.; Zhou, B.; Ellrod, G.; Minnis, P.; Trier, S.; Griffin, S.; Yum, S.S.; Gharabaghi, B.; et al. A review of high impact weather for aviation meteorology. *Pure Appl. Geoph.* **2019**, *176*, 1869–1921. [CrossRef]
28. Dee, D.P.; Uppala, S.M.; Simmons, A.J.; Berrisford, P.; Poli, P.; Kobayashi, S.; Andrae, U.; Balmaseda, M.A.; Balsamo, G.; Bauer, P.; et al. The ERA-Interim reanalysis: Configuration and performance of the data assimilation system. *Q. J. R. Met. Soc.* **2011**, *137*, 553–597. [CrossRef]

29. Kalnay, E.; Kanamitsu, M.; Kistler, R.; Collins, W.; Deaven, D.; Gandin, L.; Iredell, M.; Saha, S.; White, G.; Woollen, J.; et al. The NCEP/NCAR 40-year reanalysis project. *BAMS* **1996**, *77*, 437–471. [CrossRef]
30. Gelaro, R.; McCarty, W.; Suárez, M.J.; Todling, R.; Molod, A.; Takacs, L.; Randles, C.A.; Darmenov, A.; Bosilovich, M.G.; Reichle, R.; et al. The modern-era retrospective analysis for research and applications, version 2 (MERRA-2). *J. Clim.* **2017**, *30*, 5419–5454. [CrossRef]
31. Hersbach, H.; Bell, B.; Berrisford, P.; Hirahara, S.; Horányi, A.; Muñoz-Sabater, J.; Nicolas, J.; Peubey, C.; Radu, R.; Schepers, D.; et al. The ERA5 global reanalysis. *Q. J. R. Met. Soc.* **2020**, *146*. [CrossRef]
32. Saha, S.; Moorthi, S.; Pan, H.-L.; Wu, X.; Wang, J.; Nadiga, S.; Tripp, P.; Kistler, R.; Woollen, J.; Behringer, D.; et al. The NCEP climate forecast system reanalysis. *BAMS* **2010**, *91*, 1015. [CrossRef]
33. Bromwich, D.; Kuo, Y.H.; Serreze, M.; Walsh, J.; Bai, L.S.; Barlage, M.; Hines, K.; Slater, A. Arctic system reanalysis: Call for community involvement. *Eos. Trans. AGU* **2010**, *91*, 13–14. [CrossRef]
34. Bromwich, D.; Wilson, A.B.; Bai, L.; Liu, Z.; Barlage, M.; Shih, C.-F.; Maldonado, S.; Hines, K.M.; Wang, S.-H.; Woollen, J.; et al. The Arctic System Reanalysis, Version 2. *BAMS* **2018**, *99*, 805–828. [CrossRef]
35. Hines, K.M.; Bromwich, D.H. Development and testing of Polar WRF. Part I: Greenland ice sheet meteorology. *Mon. Weather Rev.* **2008**, *136*, 1971–1989. [CrossRef]
36. Bromwich, D.H.; Wilson, A.B.; Bai, L.S.; Moore, G.W.K.; Bauer, P. A comparison of the regional Arctic System Reanalysis and the global ERA-Interim Reanalysis for the Arctic. *Q. J. R. Met. Soc.* **2016**, *142*, 644–658. [CrossRef]
37. Varentsov, M.I.; Verezemskaya, P.S.; Zabolotskikh, E.V.; Repina, I.A. Quality estimation of polar lows reproduction based on reanalysis data and regional climate modelling. *Sovr. Problemy Distanc. Zondir. Zemli iz Kosmosa* **2016**, *13*, 168–191. [CrossRef]
38. Gavrikov, A.; Gulev, S.K.; Markina, M.; Tilinina, N.; Verezemskaya, P.; Barnier, B.; Dufour, A.; Zolina, O.; Zyulyaeva, Y.; Krinitskiy, M.; et al. RAS-NAAD: 40-yr High-Resolution North Atlantic Atmospheric Hindcast for Multipurpose Applications (New Dataset for the Regional Mesoscale Studies in the Atmosphere and the Ocean). *J. Appl. Met. Clim.* **2020**, *59*, 793–817. [CrossRef]
39. Verezemskaya, P.S.; Stepanenko, V.M. Numerical simulation of the structure and evolution of a polar mesocyclone over the Kara Sea. Part 1. Model validation and estimation of instability mechanisms. *Russ. Meteorol. Hydrol.* **2016**, *41*, 425–434. [CrossRef]
40. Diansky, N.; Fomin, V.; Kabatchenko, I.; Gusev, A. Numerical simulation of circulation in Kara and Pechora Seas using the system of operational diagnosis and forecast of the marine dynamics. *EGUGA* **2015**, *4*, 13370.
41. Semenov, A.; Zhang, X.; Rinke, A.; Dorn, W.; Dethloff, K. Arctic intense summer storms and their impacts on sea ice—A regional climate modeling study. *Atmosphere* **2019**, *10*, 218. [CrossRef]
42. Information about CLM-Community. Available online: https://wiki.coast.hzg.de/clmcom (accessed on 15 August 2020).
43. Böhm, U.; Kücken, M.; Ahrens, W.; Block, A.; Hauffe, D.; Keuler, K.; Rockel, B.; Will, A. CLM–The Climate Version of LM: Brief Description and Long-Term Applications. *COSMO Newslett.* **2006**, *6*, 225–235.
44. Rockel, B.; Geyer, B. The performance of the regional climate model CLM in different climate regions, based on the example of precipitation. *Met. Zeitsch.* **2008**, *17*, 487–498. [CrossRef]
45. Arakawa, A.; Lamb, V.R. Computational design of the basic dynamical processes of the UCLA general circulation model. *Meth. Comp. Phys.* **1977**, *17*, 173–265.
46. Gal-Chen, T.; Somerville, R.C.J. On the use of a coordinate transformation for the solution of the Navier-Stokes equations. *J. Comp. Phys.* **1975**, *17*, 209–228. [CrossRef]
47. Schär, C.; Leuenberger, D.; Fuhrer, O.; Lüthi, D.; Girard, C. A new terrain-following vertical coordinate formulation for atmospheric prediction models. *Mon. Weather Rev.* **2002**, *130*, 2459–2480. [CrossRef]
48. Ritter, B.; Geleyn, J.F. A comprehensive radiation scheme for numerical weather prediction models with potential applications in climate simulations. *Mon. Weather Rev.* **1992**, *120*, 303–325. [CrossRef]
49. Tiedtke, M. A comprehensive mass flux scheme for cumulus parameterization in large-scale models. *Mon. Weather Rev.* **1989**, *117*, 1779–1800. [CrossRef]
50. Klemp, J.B.; Durran, D.R. An upper boundary condition permitting internal gravity wave radiation in numerical mesoscale models. *Mon. Weather Rev.* **1983**, *111*, 430–444. [CrossRef]
51. Skamarock, W.C.; Klemp, J.B. The stability of time-split numerical methods for the hydrostatic and the nonhydrostatic elastic equations. *Mon. Weather Rev.* **1992**, *120*, 2109–2127. [CrossRef]

52. Core Documentation of the COSMO Model. Available online: http://www.cosmo-model.org/content/model/documentation/core/default.htm (accessed on 9 August 2020).
53. Asensio, H.; Messmer, M.; Lüthi, D.; Osterried, K. External Parameters for Numerical Weather Prediction and Climate Application EXTPAR v5_0. User and Implementation Guide. Available online: http://www.cosmo-model.org/content/support/software/ethz/EXTPAR_user_and_implementation_manual_202003.pdf (accessed on 16 November 2018).
54. Schulz, J.-P.; Heise, E. A new scheme for diagnosing near-surface convective gusts. *COSMO Newslett.* **2003**, *3*, 221–225.
55. Platonov, V.S.; Varentsov, M.I. Supercomputer technologies as a tool for high-resolution atmospheric modelling towards the climatological timescales. *Supercomp. Front. Innov.* **2018**, *5*, 107–110. [CrossRef]
56. Chen, F.; von Storch, H. Trends and Variability of North Pacific Polar Lows. *Adv. Met.* **2013**, *13*, 1–11. [CrossRef]
57. Haas, R.; Pinto, J.G. A combined statistical and dynamical approach for downscaling large-scale footprints of European windstorms. *GRL* **2012**, *39*, 1–6. [CrossRef]
58. Kotlarski, S.; Keuler, K.; Christensen, O.B.; Colette, A.; Déqué, M.; Gobiet, A.; Goergen, K.; Jacob, D.; Lüthi, D.; van Meijgaard, E.; et al. Regional climate modeling on European scales: A joint standard evaluation of the EURO-CORDEX RCM ensemble. *Geosci. Model. Dev.* **2014**, *7*, 1297–1333. [CrossRef]
59. Geyer, B. High-resolution atmospheric reconstruction for Europe 1948–2012: CoastDat2. *Earth Syst. Sci. Data* **2014**, *6*, 147–164. [CrossRef]
60. Hackenbruch, J.; Schädler, G.; Schipper, J.W. Added value of high-resolution regional climate simulations for regional impact studies. *Met. Zeitsch.* **2016**, *25*, 291–304. [CrossRef]
61. Keuler, K.; Radtke, K.; Kotlarski, S.; Lüthi, D. Regional climate change over Europe in COSMO-CLM: Influence of emission scenario and driving global model. *Met. Zeitsch.* **2016**, 121–136. [CrossRef]
62. Kislov, A.V.; Rivin, G.S.; Platonov, V.S.; Varentsov, M.I.; Rozinkina, I.A.; Nikitin, M.A.; Chumakov, M.M. Mesoscale atmospheric modeling of extreme velocities over the sea of Okhotsk and Sakhalin. *Izv. Atm. Ocean. Phys.* **2018**, *54*, 322–326. [CrossRef]
63. Platonov, V.; Kislov, A.; Rivin, G.; Varentsov, M.; Rozinkina, I.; Nikitin, M.; Chumakov, M. Mesoscale atmospheric modelling technology as a tool for creating a long-term meteorological dataset. *IOP Conf. Series Earth Env. Sci.* **2017**, *96*. [CrossRef]
64. Platonov, V.; Varentsov, M. Creation of the long-term high-resolution hydrometeorological archive for Russian Arctic: Methodology and first results. *IOP Conf. Series Earth Env. Sci.* **2019**, *386*. [CrossRef]
65. Luettich, R.A.; Westerink, J.J. Formulation and Numerical Implementation of the 2D/3D ADCIRC Finite Element Model Version 44.XX. p. 74. Available online: https://www.aquaveo.com/software/sms-adcirc (accessed on 4 October 2020).
66. Bucchignani, E.; Montesarchio, M.; Zollo, A.L.; Mercogliano, P. High-resolution climate simulations with COSMO-CLM over Italy: Performance evaluation and climate projections for the 21st century. *Int. J. Clim.* **2016**, *6*, 735–756. [CrossRef]
67. Parkinson, C.L.; Comiso, J.C. On the 2012 record low Arctic sea ice cover: Combined impact of preconditioning and an August storm. *Geophys. Res. Lett.* **2013**, *40*, 1356–1361. [CrossRef]
68. Stopa, J.E.; Ardhuin, F.; Girard-Ardhuin, F. Wave climate in the Arctic 1992–2014: Seasonality and trends. *Cryosphere* **2016**, *10*. [CrossRef]
69. Screen, J.A.; Simmonds, I.; Keay, K. Dramatic interannual changes of perennial Arctic sea ice linked to abnormal summer storm activity. *J. Geophys. Res.* **2011**, *116*, D15105. [CrossRef]
70. Von Storch, H.; Langenberg, H.; Feser, F. A spectral nudging technique for dynamical downscaling purposes. *Mon. Weather Rev.* **2000**, *128*, 3664–3673. [CrossRef]
71. Feser, F.; Barcikowska, M. The influence of spectral nudging on typhoon formation in regional climate models. *Environ. Res. Lett.* **2012**, *7*, 014024. [CrossRef]
72. Miguez-Macho, G.; Stenchikov, G.L.; Robock, A. Spectral nudging to eliminate the effects of domain position and geometry in regional climate model simulations. *J. Geophys. Res. Atmos.* **2004**, *109*. [CrossRef]
73. Hofherr, T.; Kunz, M. Extreme wind climatology of winter storms in Germany. *Clim. Res.* **2010**, *41*, 105–123. [CrossRef]

74. Panitz, H.J.; Schädler, G.; Feldmann, H. Modelling Regional Climate Change in Southwest Germany. In *High Performance Computing in Science and Engineering'09*; Springer: Berlin, Heidelberg, 2010; pp. 429–441. [CrossRef]
75. Marsaleix, P.; Auclair, F.; Estournel, C. Considerations on open boundary conditions for regional and coastal ocean models. *J. Atmos. Ocean. Technol.* **2006**, *23*, 1604–1613. [CrossRef]
76. Warner, T.T.; Peterson, R.A.; Treadon, R.E. A tutorial on lateral boundary conditions as a basic and potentially serious limitation to regional numerical weather prediction. *BAMS* **1997**, *78*, 2599–2618. [CrossRef]
77. Rinke, A.; Dethloff, K. On the sensitivity of a regional Arctic climate model to initial and boundary conditions. *Clim. Res.* **2000**, *14*, 101–113. [CrossRef]
78. Voevodin, V.L.; Antonov, A.; Nikitenko, D.; Shvets, P.; Sobolev, S.; Sidorov, I.; Stefanov, K.; Voevodin, V.; Zhumatiy, S. Supercomputer Lomonosov-2: Large Scale, Deep Monitoring and Fine Analytics for the User Community. *Supercomp. Front. Innov.* **2019**, *6*, 4–11. [CrossRef]
79. Bulygina, O.N.; Veselov, V.M.; Razuvaev, V.N.; Alexandrova, T.M. Database Description of the Main Meteorological Parameters on the Russian Stations: Certificate of State Register Database No. 2014620549. Reg. 10.04.2014. Available online: http://meteo.ru/data/163-basic-parameters#описание-массива-данных (accessed on 9 August 2020).
80. Efimov, V.V.; Komarovskaya, O.I. The Novaya Zemlya bora: Analysis and numerical modeling. *Izv. Atm. Ocean. Phys.* **2018**, *54*, 73–85. [CrossRef]
81. Shestakova, A.A.; Myslenkov, S.A.; Kuznetsova, A.M. Influence of Novaya Zemlya Bora on Sea Waves: Satellite Measurements and Numerical Modeling. *Atmosphere* **2020**, *11*, 726. [CrossRef]
82. Serreze, M.C.; Barrett, A.P.; Stroeve, J. Recent changes in tropospheric water vapor over the Arctic as assessed from radiosondes and atmospheric reanalyses. *J. Geophys. Res.* **2012**, *117*, D10104. [CrossRef]
83. Tilinina, N.; Gulev, S.K.; Bromwich, D.H. New view of Arctic cyclone activity from the Arctic system reanalysis. *Geophys. Res. Lett.* **2014**, *41*, 1766–1772. [CrossRef]
84. Akperov, M.; Rinke, A.; Mokhov, I.I.; Matthes, H.; Semenov, V.A.; Adakudlu, M.; Cassano, J.; Christensen, J.H.; Dembitskaya, M.A.; Dethloff, K.; et al. Cyclone activity in the Arctic from an ensemble of regional climate models (Arctic CORDEX). *J. Geophys. Res. Atmos.* **2018**, *123*, 2537–2554. [CrossRef]
85. Smith, R.B. 100 Years of Progress on Mountain Meteorology Research. *Meteo. Monogr.* **2019**, *59*, 20.1–20.73. [CrossRef]
86. Gill, A. *Atmosphere-Ocean. Dynamics*; Academic Press: New York, NY, USA, 1982; p. 662.
87. Etling, D. On Atmospheric Vortex Streets in the Wake of Large Islands. *Meteorol. Atmos. Phys.* **1989**, *41*, 157–164. [CrossRef]
88. Etling, D. Mesoscale Vortex Shedding from Large Islands: A Comparison with Laboratory Experiments of Rotating Stratified Flows. *Meteorol. Atmos. Phys.* **1990**, *43*, 145–151. [CrossRef]
89. McGinley, J.A.; Zupanski, M. Numerical Analysis of the Influence of Jets, Fronts, and Mountains on Alpine Lee Cyclogenesis: More Cases from the ALPEX SOP. *Meteorol. Atmos. Phys.* **1990**, *43*, 7–20. [CrossRef]
90. Barry, R.G. *Mountain Weather and Climate*, 3rd ed.; Cambridge University Press: Cambridge, UK, 2008; p. 532.
91. Corby, G.A. The airflow over mountains: A review of the state of current knowledge. *Q. J. R. Met. Soc.* **1954**, *80*, 491–521. [CrossRef]
92. Holton, J.R.; Hakim, G.J. *An Introduction to Dynamic Meteorology*, 5th ed.; Academic Press: New York, NY, USA, 2013; p. 532.
93. Narasimha, R.; Rao, K.N.; Badri Narayanan, M.A. "Bursts" in Turbulent Flows. *Adv. Geophys.* **1975**, *18*, 372. [CrossRef]
94. Vassilicos, J.C. *Intermittency in Turbulent Flows*; Cambridge Univ. Press: Cambridge, UK, 2001.
95. Jiménez, J. Intermittency in Turbulence. In *Encyclopedia of Mathematical Physics*; Françoise, J.-P., Naber, G.L., Tsun, T.S., Eds.; Academic Press Elsevier: Oxford, UK, 2006; pp. 144–151. [CrossRef]
96. Kislov, A.; Matveeva, T. An extreme value analysis of wind speed over the European and Siberian parts of Arctic region. *Atm. Clim. Sci.* **2016**, *6*, 205–223. [CrossRef]
97. Shestakova, A.A.; Toropov, P.A.; Matveeva, T.A. Climatology of extreme downslope windstorms in the Russian Arctic. *Wea. Clim. Extr.* **2020**, *28*, 100256. [CrossRef]

98. Durran, D.R. Another look at downslope windstorms. Part I: The development of analogs to supercritical flow in an infinitely deep, continuously stratified fluid. *J. Atmos. Sci.* **1986**, *43*, 2527–2543. [CrossRef]
99. Shestakova, A.A.; Moiseenko, K.B. Hydraulic Regimes of Flow over Mountains during Severe Downslope Windstorms: Novorossiysk Bora, Novaya Zemlya Bora, and Pevek Yuzhak. *Izv. Atmos. Ocean. Phys.* **2018**, *54*, 344–353. [CrossRef]